Proceedings of the ASME 2018 International Design Engineering Technical Conferences and Computers and Information in Engineering Conference
IDETC/CIE 2018
August 26-29, 2018, Quebec City, Quebec, Canada

DETC2018-86072

MODELING THE SELECTIVE LASER MELTING OF MULTI-COMPONENT THERMOELECTRIC POWDERS

Yongjia Wu*, Lei Zuo, Kan Sun
Virginia Tech
Blacksburg, VA, USA
Email: yjwu2015@vt.edu, leizuo@vt.edu

ABSTRACT

Thermoelectrics enables thermal and electrical energy conversion or device cooling without any moving parts. It has remained a significant challenge to manufacture compact and high performance thermoelectric modules in a large volume using the conventional methods because of their drawbacks in practice, such as the long processing time and misalignment of individual thermoelectric elements. Selective laser melting (SLM) based additive manufacturing approach might offer a unique method to fabricate the low cost, reliable, highly efficient, scalable, and environmentally friendly thermoelectric modules. To understand the thermodynamic and hydrodynamic phenomenon during the SLM processing is of critical importance to ensure high quality products. In this paper, we developed a model which can be used to guide the SLM manufacturing of thermoelectric material with other nanoparticles embedded for higher thermoelectric performance. This physical model based on the continuous equations had the ability to analyze the fluid flow driven by buoyancy force and surface tension, which can be used to analyze the influence of the process parameters on the pool size, particle segregation, as well as temperature distribution within the powder bed. This information is very useful for developing robust SLM for thermoelectric device fabrication.

NOMENCLATURE

ρ	Density ($kg \cdot m^{-3}$)
u, v, w	Velocities in x, y, z direction ($m \cdot s^{-1}$)
p	Pressure (Pa)
T	Temperature (K)
u_b	Laser moving speed ($m \cdot s^{-1}$)
C^+	Effective nano-particles concentration ratio
x, y, z	Coordinates (m)
h	Enthalpy (J)
μ^+	Effective diffusion coefficient ($kg \cdot m^{-1} \cdot s^{-1}$)
k^+	Effective thermal conductivity ($W \cdot K^{-1}$)
D^+	Effective diffusion coefficient ($m^{-2} \cdot s^{-1}$)
w_s	Relative velocity caused by the shrinkage of the porous powder bed (m/s)
β, β_s	Thermal expansion coefficient, solid particle expansion coefficient (K^{-1})
T_M	Melting temperature (K)
C_l, C_e	The solid mass concentration ratio, the eutectic mass concentration ratio
S_h, S_C	Energy source term ($J \cdot kg \cdot m^{-3} \cdot t^{-1}$), concentration source term ($kg \cdot m^{-3} \cdot t^{-1}$)
ε	Porosity
s	Shrinkage depth (m)
f_l, f_s	Mass fraction of the liquid and solid
μ_l, μ_s	Diffusion coefficients of the liquid and solid ($kg \cdot m^{-1} \cdot s^{-1}$)
k_l, k_s	Thermal conductivities of the liquid and solid ($W \cdot K^{-1}$)
k_{pi}, k_g	Thermal conductivities of the i-th powder and gas in the powder bed ($W \cdot K^{-1}$)
D_l, D_s	Diffusion coefficients of the liquid and solid ($m^{-2} \cdot s^{-1}$)
h_c	Convective heat transfer coefficient ($W \cdot K^{-1} \cdot m^2$)
c_p	Thermal capacity ($J \cdot kg^{-1} \cdot K$)
L	Latent heat ($J \cdot kg^{-1}$)

1. INTRODUCTION

The selective laser melting (SLM) process (Figure 1) [1] involves the use of a high power laser (e.g., a carbon dioxide laser) to fuse small particles of plastic, metal, ceramic, or glass powders into a mass that has a desired three-dimensional shape and physical properties. During the SLM fabrication, the laser selectively fuses powdered materials by scanning cross-sections generated from a 3-D digital description of the part (e.g., a CAD file or scan data). After each cross-section is scanned, the powder bed is lowered by one-layer thickness (1-200 μm). A new layer of material is applied on the top. The process is repeated until the part is completed. Like other additive manufacture (AM) technologies, SLM fabrication can make each individual component to whatever shape and size, thus allowing the entire unit to take shapes and forms previously impossible (or very difficult) to make. Generally, SLM has a high energy input thus

Copyright © 2018 ASME

Downloaded From: http://proceedings.asmedigitalcollection.asme.org on 11/06/2018 Terms of Use: http://www.asme.org/about-asme/terms-of-use

it can fabricate high melting-temperature material with high density (up to 99% full density) without the aid of additives for the binding purpose.

SLM process belongs to a complex 3D unsteady heat transfer problem, in which, powder changes from solid phase to liquid phase and then back to solid phase rapidly and repeatedly. Since the operation temperature of SLM is as high as 1500 °C, the control of material properties in high temperature environment is a practical problem. Varying process parameters like laser wavelength (type of laser), laser energy (i.e. power, scan speed and scan spacing) and powder characteristics directly influences the properties of resulting part, such as the surface quality or part density. A moving boundary, at which thermal energy is either absorbed or liberated, exists that separates the phases. The superheat in the melting powder and the latent heat liberated at the solid/liquid boundary is transferred across the solidified part and the boundaries. In some cases, the powders are partly solid and partly liquid and resemble a porous medium which is referred as a "mushy zone". The presence of the liquid for a short time squeezes out the air in the powder bed and leads to a shrinkage of the powder-liquid mixture. Thus, the density of the sintered material depends on the temperature evolution. When these process parameters are not correctly chosen, these powders are either not sintered at all or completely melted, joining into rather large drops.

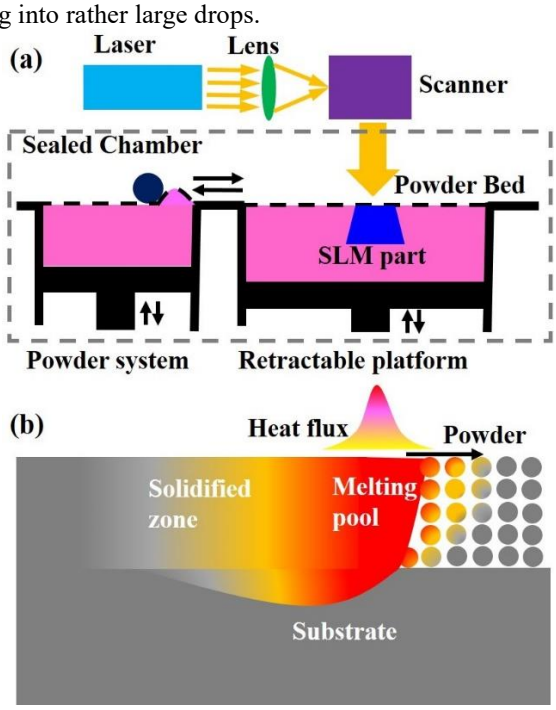

Figure 1. (a) The SLM equipment and (b) fabrication process

Temperature is the most important parameter during the SLM processing. Researchers have formulated several 3D heat transfer models to describe SLM thermal evolution [5-8]. Ahmed et al. [5] conducted a three-dimensional simulation to investigate the temperature and stress fields in single 316L stainless steel layers built on the powder bed using commercial finite element software ANSYS. Dai and Shaw [7] developed a model to analyze the effects of the volume shrinkage due to transformation from a powder compact to dense liquid on the temperature distribution and the size of the transformation zone during laser densification. The simplified model used temperature as a marker to track the fluid and powder interface. It was found that the model adequately provided good estimations of the temperature field and the size of the laser-densified body. Zhang et al. [9] built a one-dimensional thermal model to simulate the phase change phenomenon in a powder bed containing a mixture of two powders. In ref. [3], this model was expanded to a more comprehensive one to analyze a single-component metal powder bed, in which the melting processes was divided into three stages, namely the preheating stage, the first melting stage, and the second melting stage. The analytical solutions for each stages were given when taking into account the effects of shrinkage and the volume fraction of the gas during this process.

As the SLM is a complex melting and re-solidification process, in which fluid plays a vital role in the deposited material properties. The properties of the sintered materials are strongly dependent on the solidification microstructure (grain size and morphology). The bind mechanism invoked in full melting is largely driven by the fluid behavior, such as surface tension (or Raleigh instabilities), viscosity, wetting, thermo-capillary (or Marangoni convection), evaporation, and oxidation. Therefore, it is necessary to develop a sound and comprehensive physical model which has the capability to handle the detail fluid dynamics to analyze the effects of various process parameters on properties of sintered materials. To achieve this goal, researchers developed some models that had expanded abilities which took more effects into consideration. There were mainly two tools for the thermodynamic and hydrodynamic analysis of SLM process, namely conventional heat and mass transfer analysis [10, 11] and the lattice Boltzmann method [12, 13].

Since the laser sintering shared many similar characteristics with welding processing, the first SLM model was adapted from the welding simulation [14-17]. Voller and Brent [17] summarized the one-phase modeling of binary alloy solidification systems into three models according to the problem domain. These models, consistent with observations in many metallurgical systems, can predict the macro-segregation patterns during the solidification process. To better understand how the convective-diffusion process effected the temperature profile and the shape of the melting pool, Li et al. [11] established a three-dimensional numerical model for a phase change process during laser melting of ceramic materials. The binary phase diagram of the sintered ceramic material was integrated into the model to track the shape change of the melting pool. In a more comprehensive physical model developed by Xiao and Zhang [10], the shrinkage phenomena of the powder bed and the fluid flow driven by buoyancy force and surface tension gradient were taken into account. The liquid velocities caused by capillary and gravity forces and the liquid velocities caused by shrinkage were considered as well.

Lattice Boltzmann method models the fluid via a simplified time evolution of the microscopic particles [18]. This model was

Copyright © 2018 ASME

Downloaded From: http://proceedings.asmedigitalcollection.asme.org on 11/06/2018 Terms of Use: http://www.asme.org/about-asme/terms-of-use

used for some SLM process simulations because it was an economic mesoscale model which can reflect some of the underlying details in the melting and re-solidification process [12, 13]. For example, the lattice Boltzmann method has the capacity to simulate the Balling effect, an unfavorable effect which is caused by the surface tension force during the SLM manufacturing. Körner et al. [12] established a 2D lattice Boltzmann model to investigate the melting and re-solidification of a randomly packed powder bed using a Gaussian beam. This approach included many physical phenomena which cannot be described in a standard continuum picture, e.g. wetting phenomena and balling effect. Khairallah and Anderson [13] developed a 3D mesoscopic model to simulate SLM process using the ALE3D multiphysics code based on the lattice Boltzmann method. The code had the ability to predict the Plateau–Rayleigh instability during the laser scanning. The simulations gave some new physical insight that should be useful for the development of continuum models.

Thermoelectric generator is a solid state thermal engine for thermal and electrical energy conversion using electrons and holes as the working fluid [19]. In the recent years, people proposed SLM for thermoelectric material fabrication due to the desired characteristics illustrated above. In addition, during the SLM processing, it is convenient to implement grade doping and chemical composition adjustment. As a result, the ZT value of the thermoelectric material might further be improved. Wu et al. [20] proposed an optimization method for a high-efficient segmented thermo-element design, where the cross-sectional area varied along the thermo-element. This complicate design can only be fabricated by additive manufacture, such as SLM. Meanwhile, SLM integrated with nanostructured TE materials, such as nanocomposites, offers unprecedented opportunities of manipulating electron and phonon transport for a significant figure of merit (ZT) enhancement [21-24]. According to the recent research done by Tang et al. [25], the n-type $Bi_2Te_{2.7}Se_{0.3}$ fabricated by laser sintering achieved an averaged ZT of ~0.7, which was comparable to that of the corresponding material commercially available, in the temperature range of 300-550 K,. However, there is still a lack of modeling work to analyze how the microstructure of the deposited thermoelectric material will be effected by the process parameters.

In this paper, we developed a model which can be used to guide the SLM manufacturing of thermoelectric material with other nanoparticles embedded for higher thermoelectric performance. This physical model, which is used to analyze the influence of the process parameters on the pool size, particle segregation, as well as temperature distribution within the powder bed, had the ability to analyze the fluid flow driven by buoyancy force and surface tension. The governing equations, including the continuity, momentum, energy, nano-particles transport equations were solved in a pressure-based manner using a finite volume method (FVM). The total variation diminishing (TVD) discretization scheme was used to preserve second order accuracy and unconditional stability. The SIMPLER algorithm with a block correction method and an alternating direction implicit (ADI) method integrated was used to solve the discretized equations and accelerate the convergence. A grid adaptive method was used to tracking the shrinkage phenomena of the powder bed.

2. The mathematical model

2.1. The physical model

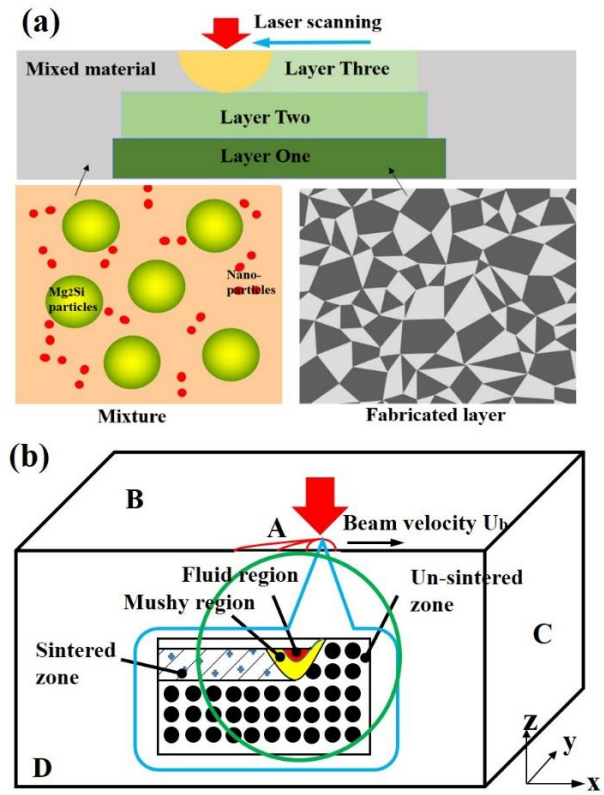

Figure 2. (a) SLM manufacturing of thermoelectric material for high ZT value; (b) The physical model for SLM simulation with a moving laser beam.

Shown in Figure 2(a) is the concept of SLM for thermoelectric material fabrication. SLM is a non-equilibrium manufacturing method, which is able to produce a lot of point defects and boundaries within the deposited material. Figure 2(b) is the physical model used for SLM simulation. A Gaussian beam is moving in the x direction with a velocity of U_b. Partition of the laser energy is absorbed by the powder and formed a liquid pool, where some nano-particles with higher melting-temperature are segregated. After the beam moving away from the sintered material, the melting pool cools down quickly and re-solidified into densified bulk part. Three distinct regions are presented in Figure 2(b), these are, a sintered region, a mushy region consisting of liquid dispersal within the solid dendrites, and a fluid region with dispersed nano-particles. This system can be accommodated by the continuum equations governing the conservation of mass, momentum, energy, and the transport of the nano-particles. The computational domain in this model is $3.6 \times 1.2 \times 1.2$ mm^3 with the melting pool has a much smaller

Copyright © 2018 ASME

Downloaded From: http://proceedings.asmedigitalcollection.asme.org on 11/06/2018 Terms of Use: http://www.asme.org/about-asme/terms-of-use

size. The temperature fluctuation far away from the melting pool is assumed to be very small. In this analysis, only half of the powder bed was simulated to save the computational resource.

2.2. Governing equations

The governing equations in this model were developed based on one-phase models descried in [10, 17], but with some modifications made to let it fit to the current problem for thermoelectric material fabrication with nano-particles embedded. Some assumptions were made to simplify the problem.

a. The porosity of the powder bed is uniform. During the sintering, the liquid will squeeze out the gas from the porous structure. In the melting pool and the sintered zone, the material become full densified. The Boussinesq approximation is used to estimate the Buoyancy force of the melted powders.
b. The thermo-physical properties (e.g. specific heat, thermal conductivities, viscosity, and diffusion coefficient) are constant, but their values might be different in the solid, mushy, and liquid regions.
c. The velocity induced by the shrinkage of the powder bed (w_s) is in the z-direction.

The laser beam moved on the powder bed with a constant speed (u_b), similar to ref. [10, 16]. The governing equations were accommodated to a one-phase model with conservation equations governing the mass, momentum, energy, and nano-particle transfer in the liquid, mushy, and solid regions in a moving coordinate system as follows.

The continuous equation

$$\frac{\partial \rho}{\partial t} + \frac{\partial(\rho u)}{\partial x} + \frac{\partial(\rho v)}{\partial y} + \frac{\partial(\rho w)}{\partial z} = 0 \tag{1}$$

The momentum equation

$$\frac{\partial(\rho u)}{\partial t} + \frac{\partial[\rho u(u-u_b)]}{\partial x} + \frac{\partial(\rho u v)}{\partial y} + \frac{\partial(\rho u(w+w_s))}{\partial z} = -\frac{\partial p}{\partial x} + \frac{\partial}{\partial x}\left(\mu^+ \frac{\partial u}{\partial x}\right) + \frac{\partial}{\partial y}\left(\mu^+ \frac{\partial u}{\partial y}\right) + \frac{\partial}{\partial z}\left(\mu^+ \frac{\partial u}{\partial z}\right) \tag{2}$$

$$\frac{\partial(\rho v)}{\partial t} + \frac{\partial[\rho v(u-u_b)]}{\partial x} + \frac{\partial(\rho v v)}{\partial y} + \frac{\partial(\rho v(w+w_s))}{\partial z} = -\frac{\partial p}{\partial y} + \frac{\partial}{\partial x}\left(\mu^+ \frac{\partial v}{\partial x}\right) + \frac{\partial}{\partial y}\left(\mu^+ \frac{\partial v}{\partial y}\right) + \frac{\partial}{\partial z}\left(\mu^+ \frac{\partial v}{\partial z}\right) \tag{3}$$

$$\frac{\partial(\rho w)}{\partial t} + \frac{\partial[\rho w(u-u_b)]}{\partial x} + \frac{\partial(\rho w v)}{\partial y} + \frac{\partial(\rho w(w+w_s))}{\partial z} = -\frac{\partial p}{\partial z} + \frac{\partial}{\partial x}\left(\mu^+ \frac{\partial w}{\partial x}\right) + \frac{\partial}{\partial y}\left(\mu^+ \frac{\partial w}{\partial y}\right) + \frac{\partial}{\partial z}\left(\mu^+ \frac{\partial w}{\partial z}\right) - \rho g[\beta_T(T-T_M) + \beta_s(C_l - C_e)] \tag{4}$$

The energy equation

$$\frac{\partial(\rho h)}{\partial t} + \frac{\partial(\rho h(u-u_b))}{\partial x} + \frac{\partial(\rho h v)}{\partial y} + \frac{\partial(\rho h(w+w_s))}{\partial z} = \frac{\partial}{\partial x}\left(k^+ \frac{\partial T}{\partial x}\right) + \frac{\partial}{\partial y}\left(k^+ \frac{\partial T}{\partial y}\right) + \frac{\partial}{\partial z}\left(k^+ \frac{\partial T}{\partial z}\right) + S_h \tag{5}$$

The nano-particle transport equation

$$\frac{\partial(\rho C^+)}{\partial t} + \frac{\partial\left(\rho C^+(u-u_b)\right)}{\partial x} + \frac{\partial(\rho C^+ v)}{\partial y} + \frac{\partial\left(\rho C^+(w+w_s)\right)}{\partial z} = \frac{\partial}{\partial x}\left(D^+ \frac{\partial C^+}{\partial x}\right) + \frac{\partial}{\partial y}\left(D^+ \frac{\partial C^+}{\partial y}\right) + \frac{\partial}{\partial z}\left(D^+ \frac{\partial C^+}{\partial z}\right) + S_C \tag{6}$$

where u, v, and w are the velocities in x, y and z direction, p is the pressure, h is the enthalpy, C^+ is the effective particle concentration, k^+ is the effective thermal conductivity, μ^+ is effective viscosity, and D^+ are the effective diffusion coefficients, S_C and S_h are source terms, β_T is the thermal expansion coefficient, β_s is the solid particle expansion coefficient, C_l is the solid mass concentration, and C_e is the eutectic mass concentration.

Because the information of eutectic temperature of the mixture of the Mg2Si powder and Si nanoparticles is missing and the Si nanoparticles play a minor role in the Buoyance force, the solid expansion term in Eq. 4 is neglected in the calculation. Like the treatment in ref. [10], w_s was the relative velocity to the coordinate system caused by the shrinkage of the porous powder bed during the melting process. To simplify the model, the porosity of the sintered material was assumed 1.0, and the density did not change during the re-solidification.

$$w_s = \begin{cases} 0, & z \geq s \\ \varepsilon\left(\frac{\partial s}{\partial t} - u_b \frac{\partial s}{\partial x}\right), & z < s \end{cases} \tag{7}$$

It was assumed that the powder starts to melt at temperature of $T_M - \Delta T$, and became fully melted at T_M. The mass fraction of the melted powder was linearly correlated to the temperature at this temperature interval (ΔT).

$$f_l = \begin{cases} 1, & T \geq T_M \\ \frac{T_M - T}{\Delta T}, & T_M - \Delta T < T < T_M \\ 0, & T < T_M - \Delta T \end{cases} \tag{8}$$

The properties of the partially melted material at the mush zone were assumed to be the summation of the liquid and the solid powder weighted by their corresponding mass fractions. The effective diffusion coefficients and the effective thermal conductivity are given by

$$\mu^+ = \mu_{eff} = \mu_s f_s + \mu_l f_l \tag{9}$$

$$k^+ = f_s k_s + f_l k_l \tag{10}$$

The powder used for SLM processing might not be pure material. For example, during the thermoelectric fabrication, doping material and additive nano-particles were mixed to enhance its ZT value. The thermal conductivity of the powder was simplified as summation of their thermal conductivity (k_{pi}) weighted by their corresponding mass fractions (g_{pi}).

$$k_p = \sum_{i=1}^{n} g_{pi} k_{pi} \tag{11}$$

For the case of a randomly packed powder bed with large thermal conductivity ratio (k_p/k_g, k_p is the particle thermal conductivity and k_g is the gas thermal conductivity), the empirical correlation proposed by Hadley [26] and further outlined in ref. [10] was used to calculate the effective thermal conductivity of the powder bed, which was given as

$$\frac{k_s}{k_g} = \frac{k_{eff}}{k_g} = (1-\alpha_0)\frac{\varepsilon f_0 + (k_p/k_g)(1-\varepsilon f_0)}{1-\varepsilon(1-f_0)+\varepsilon(k_p/k_g)(1-f_0)} + \alpha_0 \frac{2(k_p/k_g)^2(1-\varepsilon)+(1+2\varepsilon)(k_p/k_g)}{(2+\varepsilon)(k_p/k_g)+1-\varepsilon} \tag{12}$$

where

$$f_0 = 0.8 + 0.1\varepsilon, \tag{13}$$

$$\log \alpha_0 = \begin{cases} -4.898\varepsilon & 0 \leq \varepsilon \leq 0.0827 \\ -0.405 - 3.154(\varepsilon - 0.0827) & 0.0827 \leq \varepsilon \leq 0.298 \\ -1.084 - 6.778(\varepsilon - 0.298) & 0.298 \leq \varepsilon \leq 0.580 \end{cases} \tag{14}$$

Copyright © 2018 ASME

Downloaded From: http://proceedings.asmedigitalcollection.asme.org on 11/06/2018 Terms of Use: http://www.asme.org/about-asme/terms-of-use

The concentration of the additive particles in the un-sintered powder was set to be C_s. The concentration radio between the solid and the liquid was assumed to be a constant ($C_s = \varphi C_l$). The diffusive coefficient of the nano-particle within the powder was given by

$$D^+ = f_s D_s + f_l D_l / \varphi \quad (15)$$

The enthalpy of the powder was given as

$$h = \int_0^T c_{ps} dT \quad (16)$$

During the melting and solidification processes, there accompanied latent heat absorption and release. The latent heat was proportional to the mass fraction. Then the enthalpy change during the phase change is

$$\delta H = \left[\int_0^T (c_{pl} - c_{ps})\, dT + L\right] f_l \quad (17)$$

Assuming the thermal capacity of the liquid and the fully densified solid were the same, Eq. 17 can be simplified as

$$\delta H = \begin{cases} 0, & T < T_M - \Delta T \\ L f_l, & T_M - \Delta T < T < T_M \\ L, & T < T_M - \Delta T \end{cases} \quad (18)$$

The source terms for the energy equation and the particles transport equation were written in the forms similar to that used in ref. [17]. While the first term was the transient term caused by the latent heat absorption and release, the other terms were the source terms introduced by the mass convection in the melting pool.

$$S_h = \frac{-\partial}{\partial t}(\rho \delta H) - \frac{\partial}{\partial x}(\rho(u - u_b)\delta H) - \frac{\partial}{\partial y}(\rho v \delta H) - \frac{\partial}{\partial z}(\rho(w + w_s)\delta H) \quad (19)$$

$$S_C = \frac{-\partial}{\partial t}\left[\left(\frac{1}{k} - 1\right)\rho f_1 C_s\right] - \frac{\partial}{\partial x}\left[\left(\frac{1}{k} - 1\right)\rho f_1 C_s (u - u_b)\right] - \frac{\partial}{\partial y}\left[\left(\frac{1}{k} - 1\right)\rho f_1 C_s v\right] - \frac{\partial}{\partial z}\left[\left(\frac{1}{k} - 1\right)\rho f_1 C_s (w + w_s)\right] \quad (20)$$

2.3. Shrinkage tracking

Because of the porosity in the powder, when the powder melts, the liquid will occupy the air gap, forming a liquid pool with higher density. The shrinkage of powder bed introduces extra difficulty to the thermodynamic and fluid dynamic simulation for the SLM processing. In this paper, we divided the heating processes into four sub-stages to tracking the shrinkage of the melting pool.

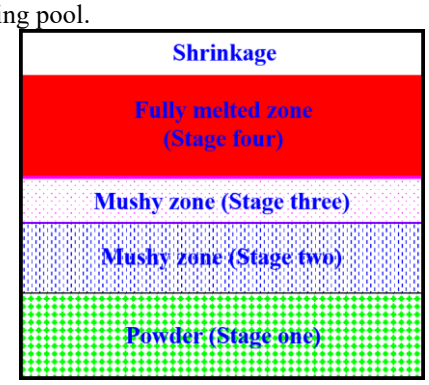

Figure 3. The shrinkage phenomenon during the SLM processing

Stage One: Pre-heating ($T < T_M - \Delta T$)

At this stage, the temperature of the heated powder is lower than the melting point. No shrinkage happens in the powder bed.

Stage Two: Preliminary melting ($T_M - \Delta T \le T \le T_M - \Delta T * \frac{\varepsilon}{1-\varepsilon}$)

At this stage, only a small partition of the powder is melted. As the liquid has higher density than the air and powder, the air gas within the powder is squeezed out by the liquid if the capillary effect is not considered. The volume of the powder melted in a local grid can be expressed as $f_l * (1 - \varepsilon) * volume(i, j, k)$. Since there is enough gas gap volume in the powder bed at this stage, the shrinkage volume in the powder equal to the melted powder volume, which is given by

$$\Delta S_1 = f_l (1 - \varepsilon) V \quad (21)$$

Stage Three: Partially melting ($T_M - \Delta T \frac{\varepsilon}{1-\varepsilon} < T < T_M$)

At this stage, the powder is still partially melted. However, as the gas within the powder is totally driven out, further melting will not lead to further shrinkage. The shrinkage at the local position equals to the volume of the powder porosity

$$\Delta S_2 = \varepsilon V \quad (22)$$

Stage Four: Fully melting ($T \ge T_M$)

At this stage, the powder is fully melted. As the density change is not taken account during the phase change process in this paper, the shrinkage in the powder bed is the same to stage three.

$$\Delta S_3 = \varepsilon V \quad (23)$$

By integrating the shrinkage of the four phases, the total shrinkage on the top of the powder bed is summarized as

$$S_{i,j} = \left(\sum_{T_M - \Delta T \frac{1-\varepsilon}{\varepsilon}}^{\infty} \varepsilon V_{i,j,k} + \sum_{T_M - \Delta T}^{T_M - \Delta T \frac{1-\varepsilon}{\varepsilon}} f_l (1 - \varepsilon) V_{i,j,k}\right) / A_{i,j} \quad (24)$$

2.4. The boundary conditions

Boundary A *(Figure 2(b)*, the heating spot*):* A Gaussian heat flux entered into the powder bed through boundary A.

$$-k_{eff} \partial T / \partial z|_{z=s} = q_{laser} + h_c (T - T_a) + \varepsilon_b \sigma_b (T^4 - T_a^4) \quad (25)$$

where the Gaussian heat flux was given by

$$q_{laser} = -\frac{q_0}{\pi R^2} exp\left(-\frac{r^2}{R^2}\right) \quad (26)$$

To model the thermo-capillary effect due to temperature gradients at the top surface, the shear force and surface tension at the free surface should equal to each other.

$$\mu^+ (\partial v_{S1} / \partial n_1 + \partial v_{n1} / \partial S_1) = \sigma_s \frac{\partial T}{\partial S_1} \quad (xz\ \ plane) \quad (27)$$

$$\mu^+ (\partial v_{S1} / \partial n_2 + \partial v_{n2} / \partial S_1) = \sigma_s \frac{\partial T}{\partial S_1} \quad (yz\ \ plane) \quad (28)$$

The nano-particle concentration boundary condition was

$$\partial C^+ / \partial z|_{z=S_1} = 0 \quad (29)$$

Boundary B (The top surface except *A*)***:*** The velocity and nano-particle concentration conditions were the same to boundary A but the thermal condition,

$$-k_{eff} \partial T / \partial z|_{z=s} = h_c (T - T_a) + \varepsilon \sigma_b (T^4 - T_a^4) \quad (30)$$

Boundary C (The right and left surface)***:*** These side and bottom surface were far away from the heat source. In addition, the thermal conductivity of the powder was very small. Thus constant temperatures were given to these surfaces,

$$T = T_a \quad (31)$$

Copyright © 2018 ASME

Downloaded From: http://proceedings.asmedigitalcollection.asme.org on 11/06/2018 Terms of Use: http://www.asme.org/about-asme/terms-of-use

$$u = v = w = 0 \quad (32)$$
$$\partial C^+/\partial x|_{z=0,L} = 0 \quad (33)$$
Boundary D (The front surface)***:*** At the symmetric surface, the boundary conditions were
$$\partial T/\partial y|_{y=0} = 0 \quad (34)$$
$$v = 0,\ \frac{\partial u}{\partial y} = \frac{\partial w}{\partial y} = 0 \quad (35)$$
$$\partial C^+/\partial y|_{y=0} = 0 \quad (36)$$

2.5. Numerical procedures

The SLM processing was a three dimensional steady state heat and mass transfer problem in the moving coordinate system. The mathematical model, specified by the continuity, momentum, energy, and nano-particle transport equations (Eqs.1-6) together with the constitutive equations (Eqs.7-20) were then solved numerically using the SIMPLER algorithm in a pressure based manner [27]. The properties of the materials were updated using the temperature obtained from the last iteration. Since the shrinkage of the powder surface was unknown, a false transient method was employed to tracking the powder bed surface. The solution was assumed to be converged when the temperature, and velocity profiles do not change with the false time. The convection and diffusion terms were discretized using a total variation diminishing (TVD) scheme developed by Van Leer [28] with the limiter function given in Eq. 37. The TVD scheme was used here because of it owned second order accuracy and was unconditional stable without overshot.

$$\psi(r) = \frac{r+|r|}{1+r} \quad (37)$$

The discretized equations using a TVD scheme in a three-dimensional Cartesian grid arrangement was extended from a two dimensional TVD scheme in ref. [29],

$$a_P\phi_P = a_W\phi_W + a_E\phi_E + a_S\phi_S + a_N\phi_N + a_F\phi_F + a_B\phi_B + S_u^{DC} + S_\phi \quad (38)$$

where $a_P, a_W, a_E, a_S, a_N, a_F, and\ a_B$ are the TVD neighbor coefficients.

The deferred correction source term in Eq. 38 was given by

$$S_u^{DC} = \frac{1}{2}F_e[(1-\alpha_e)\psi(r_e^-) - \alpha_e\psi(r_e^+)](\phi_E - \phi_P) + \frac{1}{2}F_w[-(1-\alpha_w)\psi(r_w^-) + \alpha_w\psi(r_w^+)](\phi_P - \phi_W) + \frac{1}{2}F_n[(1-\alpha_n)\psi(r_n^-) - \alpha_n\psi(r_n^+)](\phi_N - \phi_P) + \frac{1}{2}F_s[-(1-\alpha_s)\psi(r_s^-) + \alpha_s\psi(r_s^+)](\phi_P - \phi_S) + \frac{1}{2}F_b[(1-\alpha_b)\psi(r_b^-) - \alpha_b\psi(r_b^+)](\phi_B - \phi_P) + \frac{1}{2}F_f\left[-\left(1-\alpha_f\right)\psi\left(r_f^-\right) + \alpha_b\psi(r_b^+)\right](\phi_P - \phi_B) \quad (39)$$

where r_e^+, r_e^-, r_w^+, r_w^-, r_n^+, r_n^-, r_s^+, r_s^-, r_b^+, r_b^-, r_f^+, and r_f^- are defined the same to ref [29].

The additional source term method was used to treat boundary A for simplicity. The grid system used here was uniform hexahedron grids 200×90×90 (in the x, y, z directions, respectively). The false time step was 0.0005 sec. The iterative procedure was continued until the residual of each equation was less than 10^{-5}. To accelerate the convergence, the block correction method [30] and alternating direction implicit (ADI) method [29, 30] were integrated into the algorithm.

2.6. Material properties and input parameters

The numerical calculation was performed for Mg_2Si powder with Si nano-particles embedded. The thermal conductivity of the Mg_2Si was cited from the ref. [31]. Other properties, such as the thermal expansion coefficient, thermal capacity, were cited from ref. [32]. The additive material (Si particles) had a weight of 10% of the total mass. And the properties of the Si was cited from ref [33]. The material physical properties and SLM conditions were listed in table 1 as follows.

Table 1. The material physical properties and SLM conditions

Specific heat	$c_p = 67.87\ J \cdot kg^{-1} \cdot K^{-1}$
Solid thermal conductivity [31]	$k_p = 7.0\ W \cdot m^{-1} \cdot K^{-1}$
Liquid thermal conductivity	$k_l = 5.0\ W \cdot m^{-1} \cdot K^{-1}$
Gas thermal conductivity	$k_g = 0.024\ W \cdot m^{-1} \cdot K^{-1}$
Porosity	$\varepsilon = 0.2$
Density	$\rho = 1990\ kg \cdot m^{-3}$
Liquid viscosity	$\mu_l = 5.0 \times 10^{-3}\ kg \cdot m^{-1} \cdot s^{-1}$
Solid viscosity	$\mu_s = 1.0 \times 10^4\ kg \cdot m^{-1} \cdot s^{-1}$
Specific diffusion coefficient	$D = 4.8 \times 10^{-9}\ m^2 \cdot s^{-1}$
Latent heat	$L = 4.5 \times 10^5\ J \cdot kg^{-1}$
Permeability coefficient	$K_0 = 2.0 \times 10^6\ kg \cdot m^{-3} \cdot s^{-1}$
Thermal expansion coefficient	$\beta_T = 1.1 \times 10^{-5}\ K^{-1}$
Melting point of pure material	$T_M = 1375\ K$
Equilibrium partition ratio	$k = 0.8$
Ambient temperature	$T_a = 298.15\ K$
Convective heat transfer coefficient	$h_c = 10.0\ W \cdot m^{-2} \cdot K^{-1}$
Laser diameter	$R = 0.003\ m$
Boltzmann constant	$\sigma_b = 5.67 \times 10^{-8}\ W \cdot m^{-2} \cdot K^{-4}$
Change rate of surface tension	$\partial\sigma/\partial T = -10^{-5}\ kg \cdot s^{-2} \cdot K$
Laser intensity	$q_0 = 1.8 \times 10^4\ W \cdot m^{-2}$

3. Result

3.1. Code validation

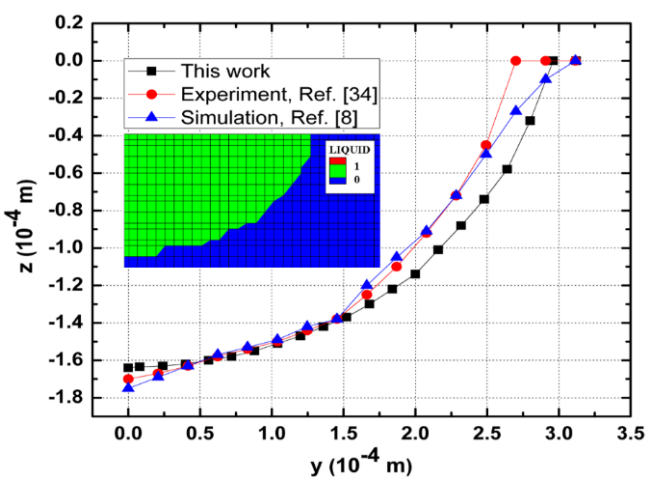

Figure 4. The comparison of the simulated and measured melting pool size for laser melting of the 6063 aluminum sheet.

Before the simulation of the multi-component powder bed, this code was used to test the processing of the nonporous 6063 aluminum sheet with dimensions of 229 × 152 × 3.2 mm^3. The

Copyright © 2018 ASME

Downloaded From: http://proceedings.asmedigitalcollection.asme.org on 11/06/2018 Terms of Use: http://www.asme.org/about-asme/terms-of-use

nominal beam power was a continuous-wave CO_2 laser with a power of 1.3 kW and a travel speed of 4.23 mm/s. The power absorbed by the work piece was measured calorimetrically. The measurement showed that about 86% of energy irradiated by the laser beam was lost via laser reflection, thermal radiation, and heat convection. The diameter of the beam was measured to be 0.6 mm. The heat flux distribution of the beam was assumed Gaussian. The physical properties of the nonporous 6063 aluminum sheet and the boundary conditions used in the simulation was the same to the ref. [34]. The result was then used to compared with the simulation result presented in ref. [10, 34] and experimental result in ref. [35]. It can be seen that the simulated and measured fusion boundaries were in good agreement with each other.

3.2. Simulation results

The validated code was then used to simulate the SLM processing of Mg_2Si powder where Si nano-particles acted as the additive material. In this case study, the laser beam had a power of 100 W, a radius of 0.3 mm, and a scanning speed of 10 mm/s. The calculation domain was 3.6 × 1.2 × 1.2 mm^3, which was large enough to represent the heat and mass transfer processes during the laser sintering. A grid system with 1.62 million uniform hexahedron cells were used for the simulation. Because of porosity existing in the powder bed, after partition of the powder was melted, the liquid squeezed out the gas filled in the powder gap. Figure 5 showed the shrinkage of the powder bed during the SLM processing. It was observed that the surface of the melting pool was not flat any more. The maximum shrinkage depth was about 0.08 mm (*D*), and the radius of the shrinkage region was about 0.54 mm (*R*) for this case. With the input power increased, the shrinkage region was expected to be larger. Due to the shrinkage phenomenon, it was a challenge to control the contact quality between the two layers of fabricated substrates.

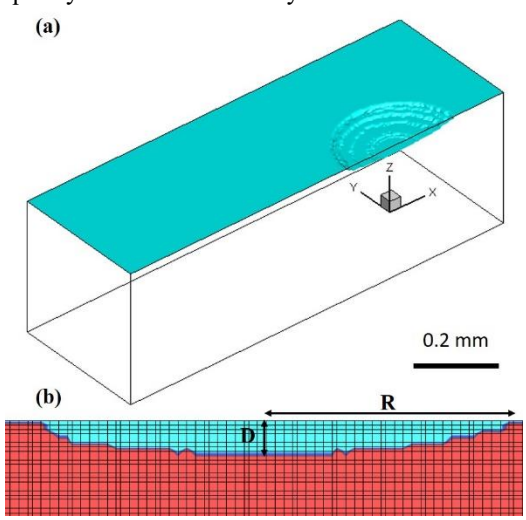

Figure 5. The shrinkage of the powder bed during the SLM processing

The melting pool size played a vital important role during the SLM processing, as the pool dynamics can significantly influence the quality of the fabricated parts. The melting and re-solidification phenomenon in the melting pool was significantly influenced by the convective heat and mass transfer processes. The marangoni and buoyancy effects, which driven the fluid circulation in the melting pool, was largely determined by the size of the melting pool. The larger melting pool should induce stronger convection during the SLM processing, which might lead to particles segregation at the boundary of the melting pool. Particles segregation was not desired to achieve uniform material properties. However, if the melting pool was too small. The powder might be fully melted. The density of the final product would be too small to sustain good electrical conductivity. A appropriate melting size should be controlled to achieve a balance. Shown in Figure 6 was the melting pool size for the current simulation case. The red region in the figure was fully melted, and the green region was solid, while the yellow and blue region was the mushy zone. The depth of the melting pool was about 0.4 mm (D), and the radius was about (R) 0.57 mm. The melting was not symmetrical as the laser beam was moving. The un-symmetricity should be more obvious for larger laser scanning speed.

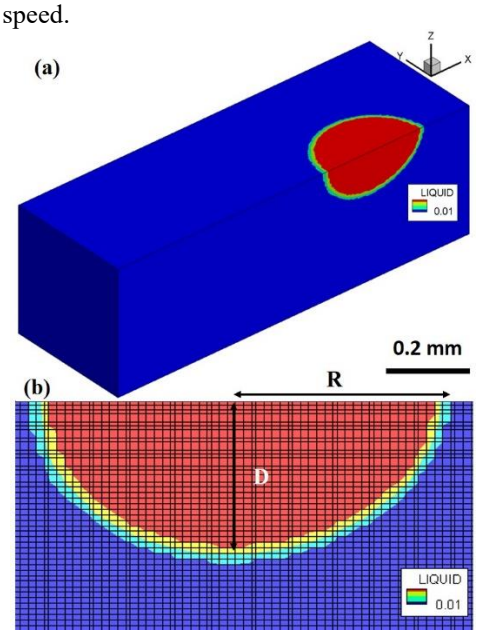

Figure 6. The melting pool size during the SLM processing

Shown in Figure 7 was the temperature profile in the powder bed during SLM processing. On the top of the melting pool, there existed a low temperature region caused by the shrinkage of the powder bed. The temperature profile was not strictly symmetrical in the *x* direction. As the laser beam moving from the left side to the right side, the high temperature region shifted slightly to the right side of the melting pool, and the heat flow penetrated deeper at the left side. The highest temperature happened at the surface of the melting pool, with a peak temperature of about 3000 K. Since the temperature of the heating surface was too high, severe evaporation might happen during the SLM processing. The input power of the laser beaming should be carefully controlled.

Copyright © 2018 ASME

Downloaded From: http://proceedings.asmedigitalcollection.asme.org on 11/06/2018 Terms of Use: http://www.asme.org/about-asme/terms-of-use

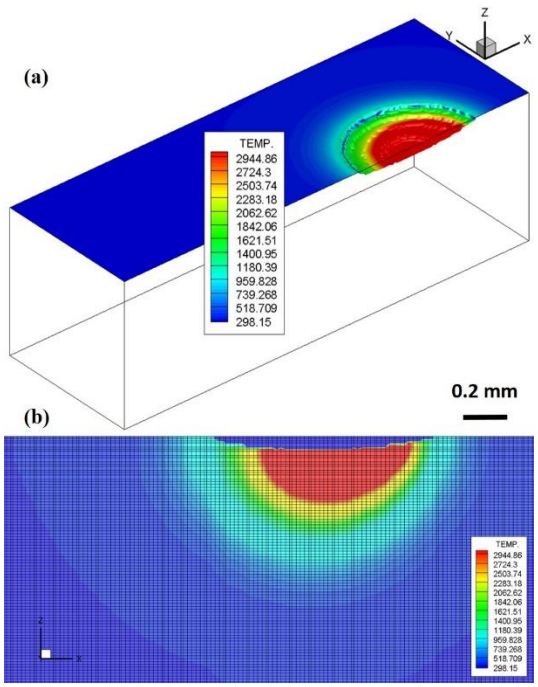

Figure 7. The temperature profile during the SLM processing

During the melting process, the non-uniformly heating of the free surface leaded to unbalanced surface tension. The thermo-capillary flow induced by surface tension variations along the liquid–gas interface together with the buoyancy force caused by the density variation drove the fluid to circulate in the melting pool. As shown in Figure 8, the circulation pattern within the melting pool was complicated. This flow pattern was generated by the combined effect of the buoyance force and the surface tension force. The surface tension force at the surface of the liquid pool tended to pull the flow from the center to the edge of the melting pool. While the buoyance force driven the flow from the bottom to the upper surface of the melting pool. With these two effects combined, a circulation was created, where the flow run up from the center and down from the edge of the melting pool. The two circulations (Figure 8 (a)) at the front face was not strictly symmetrical because of the moving laser beam, with the left circle was larger. This circulation pattern found in this paper was consistent with the patterns found in the literatures [10, 34]. The strong convection in the melting pool might accelerate the nano-particles segregation. The convection process should be carefully monitored and controlled during the processing.

Though the Si nano-particles was uniformly mixed before the SLM processing, the Si nano-particles became non-uniformly distributed after the SLM processing, as shown in Figure 8. It was observed that the nano-particles segregated at the boundary of the melting pool, while owned a lower concentration at the melting pool. This phenomenon was undesired for the thermoelectric material fabrication. As the doping level shifted from the optimum value, the performance of the thermo-electric material might be seriously deteriorated.

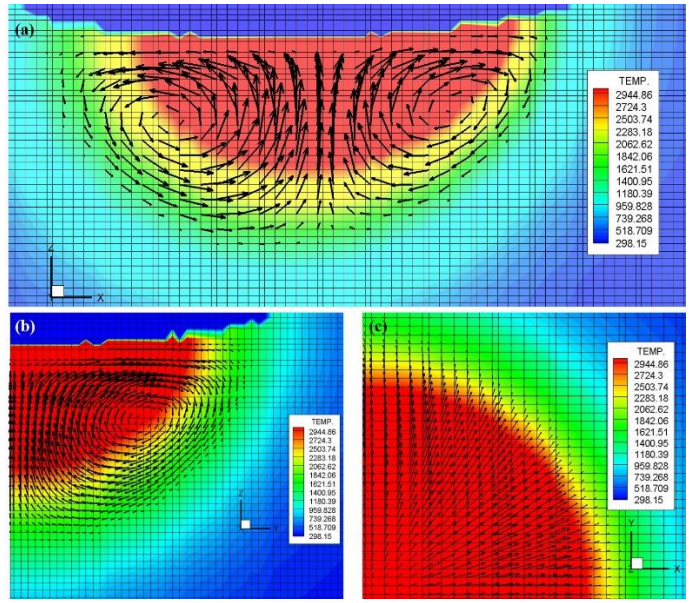

Figure 8. The velocity vector in the melting pool: (a) the front view, (b) the left view, (c) the top view.

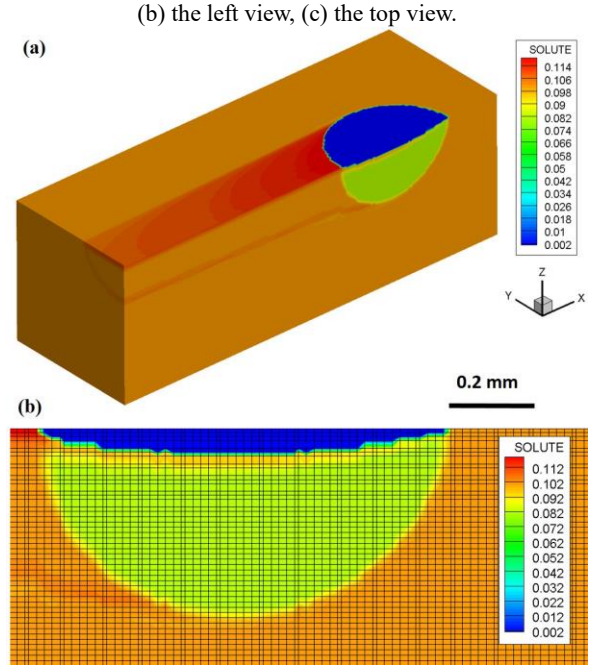

Figure 9. The solute (Si nano-particles concentration ratio) distribution during the SLM processing

4. Conclusion

In this paper, a comprehensive 3D model was developed to simulate the convection-diffusion and phase-change phenomenon during the selective laser melting of thermoelectric material (Mg_2Si) with Si nano-particles embedded. This model provided the detailed information of the shape of the melting pool, the temperature and velocity profiles, and the nano-particles concentration ratio in the powder bed. The code was validated by testing a case reported in the literature. The simulation results showed that the flow circulation induced by the surface tension and buoyancy force within the melting pool

Copyright © 2018 ASME

Downloaded From: http://proceedings.asmedigitalcollection.asme.org on 11/06/2018 Terms of Use: http://www.asme.org/about-asme/terms-of-use

matched well with literatures. The segregation of the nano-particles at the boundary of the melting pool might deteriorate the performance of the fabricated thermoelectric material.

ACKNOWLEDGMENTS

The authors gratefully acknowledge financial support from the US Department of Energy via Grant #16-10884.

REFERENCE

[1] Bremen, S., Meiners, W., and Diatlov, A., 2012, "Selective laser melting," Laser Technik Journal, 9(2), pp. 33-38.

[2] Zeng, K., Pal, D., and Stucker, B., "A review of thermal analysis methods in Laser Sintering and Selective Laser Melting," Proc. Proceedings of Solid Freeform Fabrication Symposium Austin, TX, pp. 796-814.

[3] Xiao, B., and Zhang, Y. W., 2007, "Analysis of partial melting in metal powder bed with constant heat flux," Heat Transfer Eng, 28(5), pp. 472-483.

[4] Roberts, I. A., Wang, C. J., Esterlein, R., Stanford, M., and Mynors, D. J., 2009, "A three-dimensional finite element analysis of the temperature field during laser melting of metal powders in additive layer manufacturing," Int J Mach Tool Manu, 49(12-13), pp. 916-923.

[5] Hussein, A., Hao, L., Yan, C. Z., and Everson, R., 2013, "Finite element simulation of the temperature and stress fields in single layers built without-support in selective laser melting," Mater Design, 52, pp. 638-647.

[6] Zhang, D. Q., Cai, Q. Z., Liu, J. H., Zhang, L., and Li, R. D., 2010, "Select laser melting of W-Ni-Fe powders: simulation and experimental study," Int J Adv Manuf Tech, 51(5-8), pp. 649-658.

[7] Dal, K., and Shaw, L., 2005, "Finite element analysis of the effect of volume shrinkage during laser densification," Acta Mater, 53(18), pp. 4743-4754.

[8] Fu, C. H., and Guo, Y. B., 2014, "Three-Dimensional Temperature Gradient Mechanism in Selective Laser Melting of Ti-6Al-4V," J Manuf Sci E-T Asme, 136(6).

[9] Zhang, Y. W., and Faghri, A., 1999, "Melting of a subcooled mixed powder bed with constant heat flux heating," Int J Heat Mass Tran, 42(5), pp. 775-788.

[10] Xiao, B., and Zhang, Y. W., 2007, "Marangoni and buoyancy effects on direct metal laser sintering with a moving laser beam," Numer Heat Tr a-Appl, 51(8), pp. 715-733.

[11] Li, J. F., Li, L., and Stott, F. H., 2004, "A three-dimensional numerical model for a convection-diffusion phase change process during laser melting of ceramic materials," Int J Heat Mass Tran, 47(25), pp. 5523-5539.

[12] Korner, C., Attar, E., and Heinl, P., 2011, "Mesoscopic simulation of selective beam melting processes," J Mater Process Tech, 211(6), pp. 978-987.

[13] Khairallah, S. A., and Anderson, A., 2014, "Mesoscopic simulation model of selective laser melting of stainless steel powder," J Mater Process Tech, 214(11), pp. 2627-2636.

[14] Kim, W. H., Fan, H. G., and Na, S. J., 1997, "Effect of various driving forces on heat and mass transfer in arc welding," Numer Heat Tr a-Appl, 32(6), pp. 633-652.

[15] Chakraborty, N., Chakraborty, S., and Dutta, P., 2004, "Three-dimensional modeling of turbulent weld pool convection in GTAW processes," Numer Heat Tr a-Appl, 45(4), pp. 391-413.

[16] Dutta, P., Joshi, Y., and Janaswamy, R., 1995, "Thermal Modeling of Gas Tungsten Arc-Welding Process with Nonaxisymmetric Boundary-Conditions," Numer Heat Tr a-Appl, 27(5), pp. 499-518.

[17] Voller, V. R., Brent, A. D., and Prakash, C., 1989, "The Modeling of Heat, Mass and Solute Transport in Solidification Systems," Int J Heat Mass Tran, 32(9), pp. 1719-1731.

[18] Bao, Y. B., and Meskas, J., 2011, "Lattice boltzmann method for fluid simulations," Department of Mathematics, Courant Institute of Mathematical Sciences, New York University.

[19] Rowe, D. M., 2005, Thermoelectrics handbook: macro to nano, CRC press.

[20] Wu, Y., Yang, J., Chen, S., and Zuo, L., 2018, "Thermo-element geometry optimization for high thermoelectric efficiency," Energy.

[21] Mingo, N., Hauser, D., Kobayashi, N. P., Plissonnier, M., and Shakouri, A., 2009, ""Nanoparticle-in-Alloy" Approach to Efficient Thermoelectrics: Silicides in SiGe," Nano Lett, 9(2), pp. 711-715.

[22] Wang, S. Y., Yang, J., Toll, T., Yang, J. H., Zhang, W. Q., and Tang, X. F., 2015, "Conductivity-limiting bipolar thermal conductivity in semiconductors," Sci Rep-Uk, 5.

[23] Poudel, B., Hao, Q., Ma, Y., Lan, Y. C., Minnich, A., Yu, B., Yan, X. A., Wang, D. Z., Muto, A., Vashaee, D., Chen, X. Y., Liu, J. M., Dresselhaus, M. S., Chen, G., and Ren, Z. F., 2008, "High-thermoelectric performance of nanostructured bismuth antimony telluride bulk alloys," Science, 320(5876), pp. 634-638.

[24] Minnich, A. J., Dresselhaus, M. S., Ren, Z. F., and Chen, G., 2009, "Bulk nanostructured thermoelectric materials: current research and future prospects," Energ Environ Sci, 2(5), pp. 466-479.

[25] Mao, Y., Yan, Y. G., Wu, K. P., Xie, H. Y., Xiu, Z. K., Yang, J. H., Zhang, Q. J., Uher, C., and Tang, X. F., 2017, "Non-equilibrium synthesis and characterization of n-type Bi2Te2.7Se0.3 thermoelectric material prepared by rapid laser melting and solidification," Rsc Adv, 7(35), pp. 21439-21445.

[26] Hadley, G. R., 1986, "Thermal-Conductivity of Packed Metal Powders," Int J Heat Mass Tran, 29(6), pp. 909-920.

[27] Patankar, S., 1980, Numerical heat transfer and fluid flow, CRC press.

[28] Van Leer, B., 1974, "Towards the ultimate conservative difference scheme. II. Monotonicity and conservation combined in a second-order scheme," Journal of computational physics, 14(4), pp. 361-370.

[29] Versteeg, H. K., and Malalasekera, W., 2007, An introduction to computational fluid dynamics: the finite volume method, Pearson Education.

[30] Tao, W., 2001, Numerical heat transfer (Second edition), Xi'an Jiaotong University Press.

[31] Akasaka, M., Iida, T., Matsumoto, A., Yamanaka, K., Takanashi, Y., Imai, T., and Hamada, N., 2008, "The

Copyright © 2018 ASME

Downloaded From: http://proceedings.asmedigitalcollection.asme.org on 11/06/2018 Terms of Use: http://www.asme.org/about-asme/terms-of-use

thermoelectric properties of bulk crystalline n- and p-type Mg2Si prepared by the vertical Bridgman method," J Appl Phys, 104(1).
[32] Yu, B. H., Chen, D., Tang, Q. B., Wang, C. L., and Shi, D. H., 2010, "Structural, electronic, elastic and thermal properties of Mg2Si," J Phys Chem Solids, 71(5), pp. 758-763.
[33] Glassbrenner, C., and Slack, G. A., 1964, "Thermal conductivity of silicon and germanium from 3 K to the melting point," Physical Review, 134(4A), p. A1058.
[34] Kou, S., and Wang, Y., 1986, "Three-dimensional convection in laser melted pools," Metallurgical transactions A, 17(12), pp. 2265-2270.
[35] Kou, S., and Wang, Y., 1986, "Weld pool convection and its effect," Weld. J, 65(3), pp. 63s-70s.

Copyright © 2018 ASME

Downloaded From: http://proceedings.asmedigitalcollection.asme.org on 11/06/2018 Terms of Use: http://www.asme.org/about-asme/terms-of-use